Concurrent modification of under-surface reconstruction and additional coating layers via simple Phosphoric Acid Treatment for high-stability Li-rich Cathodes in Li–ion Batteries

Yunho Noh[a], Yeonghun Park[a], Wonchang Choi[a, *]

[a]Department of Energy Engineering, Konkuk University, 120, Neungdong-ro, Gwangjin-gu, Seoul 05029, Republic of Korea

Corresponding author

Wonchang Choi / Ph. D.

Email: wcchoi@konkuk.ac.kr

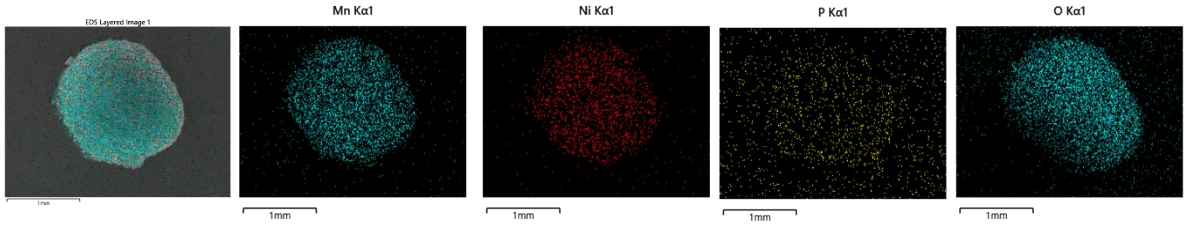

Fig. S1. SEM−EDS mapping images of Mn, Ni, P, O in the LLO@S@LP3.

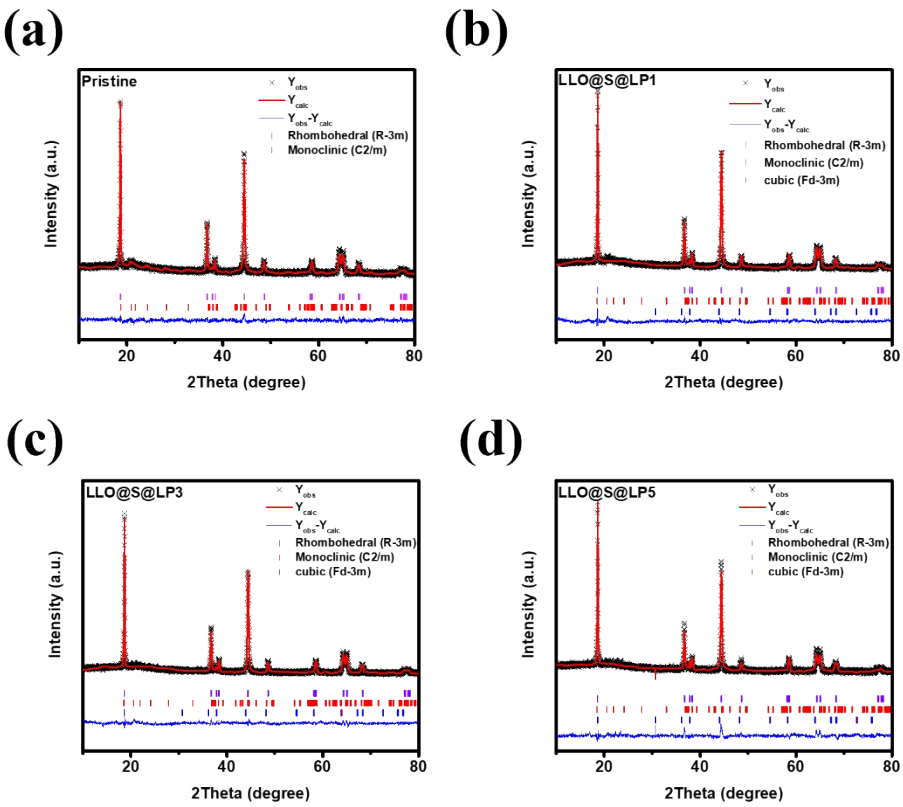

Fig. S2. XRD Rietveld Refinements data of the (a) Pristine, (b) LLO@S@LP1, (c) LLO@S@LP3, and (d) LLO@S@LP5.

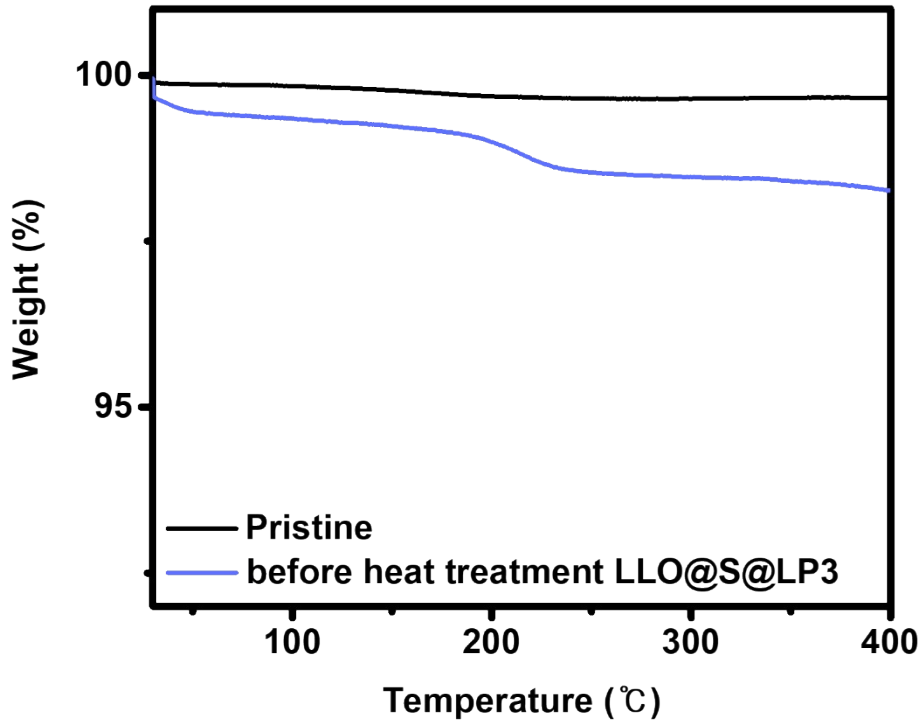

Fig. S3. Thermogravimetric analysis (TGA) data of the bare material and after ion-exchanged sample (LLO@S@LP3).

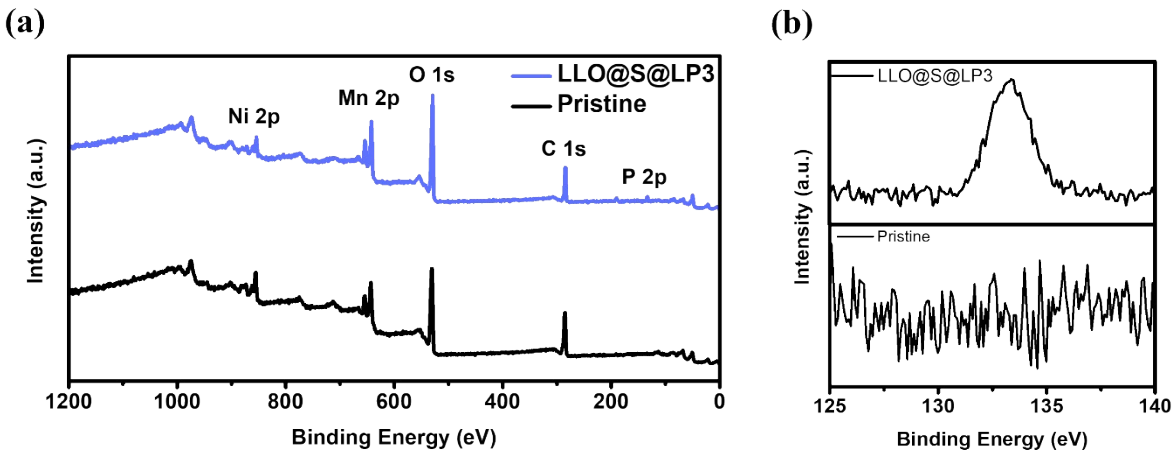

Fig. S4. (a) X-ray photoelectron spectroscopy (XPS) surveys of the pristine and LLO@S@LP3 samples. (b) XPS spectra of the P 2p for the pristine and LLO@S@LP3.

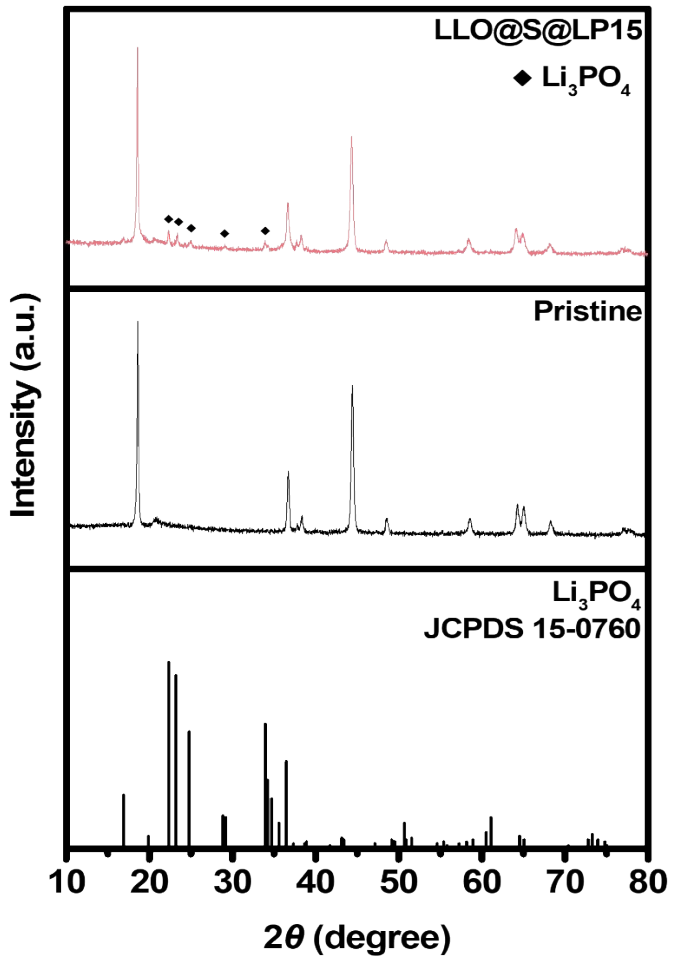

Fig. S5. X-ray diffraction (XRD) patterns of Li_3PO_4, Pristine and LLO@S@LP15

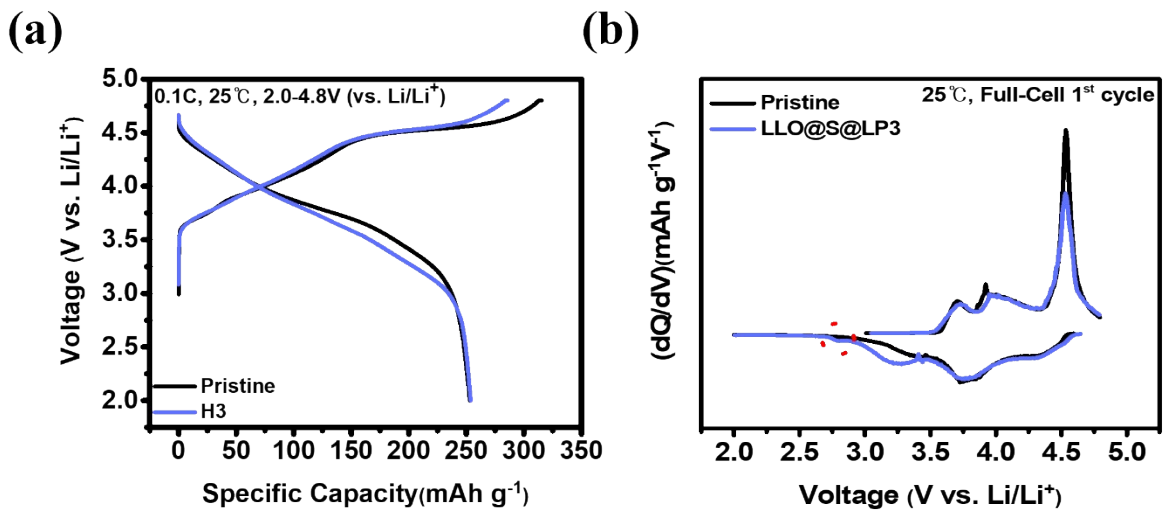

Fig. S6. Full-cell (a) Voltage profile and (b) dQ/dV of the Pristine and LLO@S@LP3.

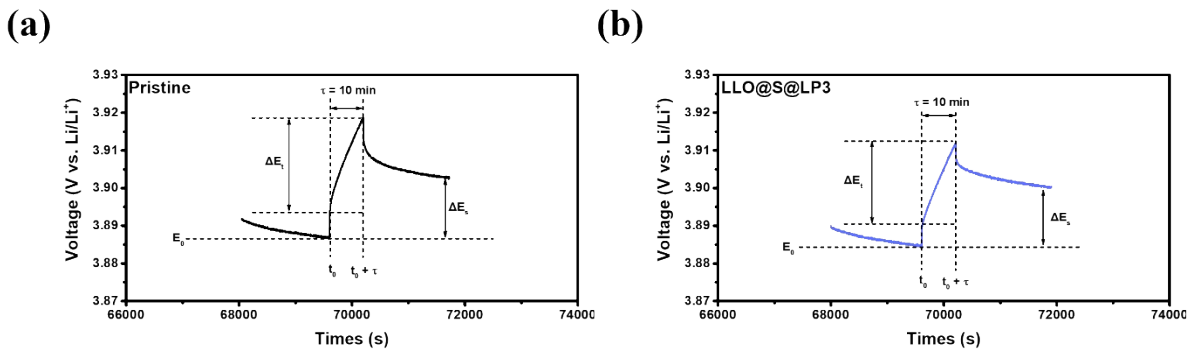

Fig. S7. (a) Potential profiles, Li–ion diffusion coefficient calculated by the galvanostatic intermittent titration technique (GITT). The (b) charging, and (c) discharging, stages.

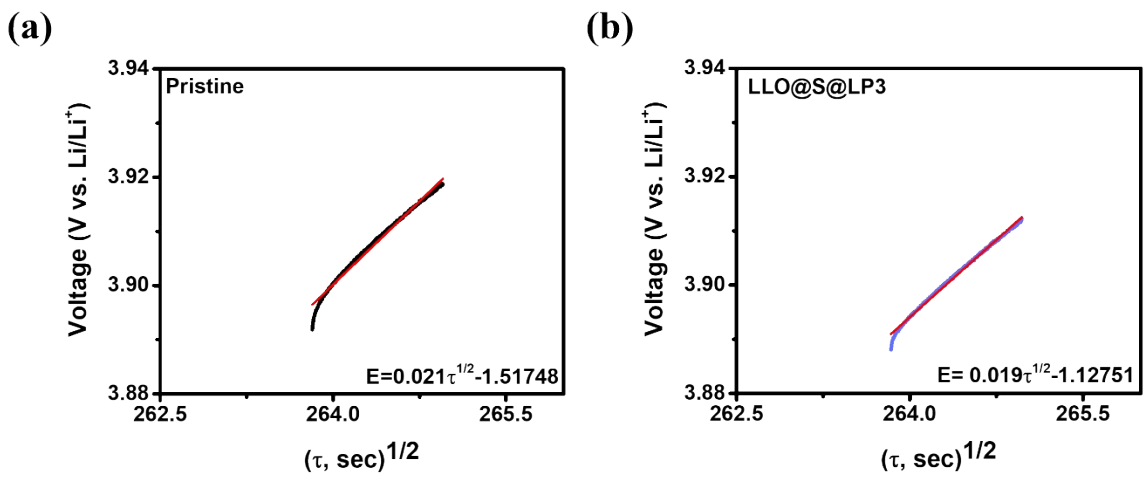

Fig. S8. Linear relationship of E *vs.* $\tau^{1/2}$ for the (a) pristine and (b) LLO@S@LP3.

Through GITT analysis, D_{Li+} was determined as follows. GITT curves were obtained in the voltage range (2.5 − 4.3) V (*vs.* Li/Li^+) after the first 0.1 C charge/discharge cycle. During charging, a constant current of 0.1 C was applied for 10 min, followed by a 30 min rest period, repeated until reaching 4.3 V, after which the system switched to the discharge state. The discharge followed a similar procedure with repeated steps.

Figure 6(a) shows the GITT curve obtained through this process, while Figs. S6(a) and (b) of the SI represent single-step voltage profiles for the pristine and LLO@S@LP3 cells in the

range (3.88 − 3.94) V (*vs.* Li/Li^+). The height of the voltage curve during the 10 min constant current application represents dE_τ, while the voltage difference between τ_0 (s), corresponding to the voltage before the constant current application, and τ_0+2,400 (s), represents dE_S.

By analyzing the voltage changes during the 10 min constant current application and 30 min rest periods, values for dE_τ and dE_S were obtained. Using these values, the diffusivity of Li^+ (D_{Li+}) for each voltage range could be calculated. D_{Li+} can be computed using Fick's second law by the following equation:

$$D_{Li^+} = \frac{4}{\pi}\left(\frac{m_B V_M}{M_B A}\right)^2 \left(\frac{\Delta E_S}{\tau\left(\frac{dE_\tau}{d\sqrt{\tau}}\right)}\right)^2 \quad (\tau \ll \frac{L^2}{D_{Li^+}})$$

Eq. (1)

where, τ (s) represents the flux time; m_B (g) and V_M ($cm^3 \cdot mol^{-1}$) are the mass loading on the electrode and the molar volume per mole, respectively; M_B (g/mol) is the molecular weight of the samples; A (cm^2) is the electrode–electrolyte contact area obtained through the Brunauer–Emmett–Teller analysis (BET); L (cm) is the electrode thickness; E_τ is the voltage during constant current application; and E_S is the voltage during the rest period.

Finally, if the relationship between E and $\tau^{1/2}$ is linear during a single GITT titration, Eq. (1) can be summarized as follows:

$$D_{Li^+} = \frac{4}{\pi\tau}\left(\frac{m_B V_M}{M_B A}\right)^2 \left(\frac{\Delta E_S}{\Delta E_\tau}\right)^2 \quad (\tau \ll \frac{L^2}{D_{Li^+}})$$

Eq. (2)

As observed in Figs. S7(a) and (b), the E *vs.* $\tau^{1/2}$ for a single step follows a straight line, and by substituting this into Eq. (2), D_{Li+} for each voltage range could be determined.

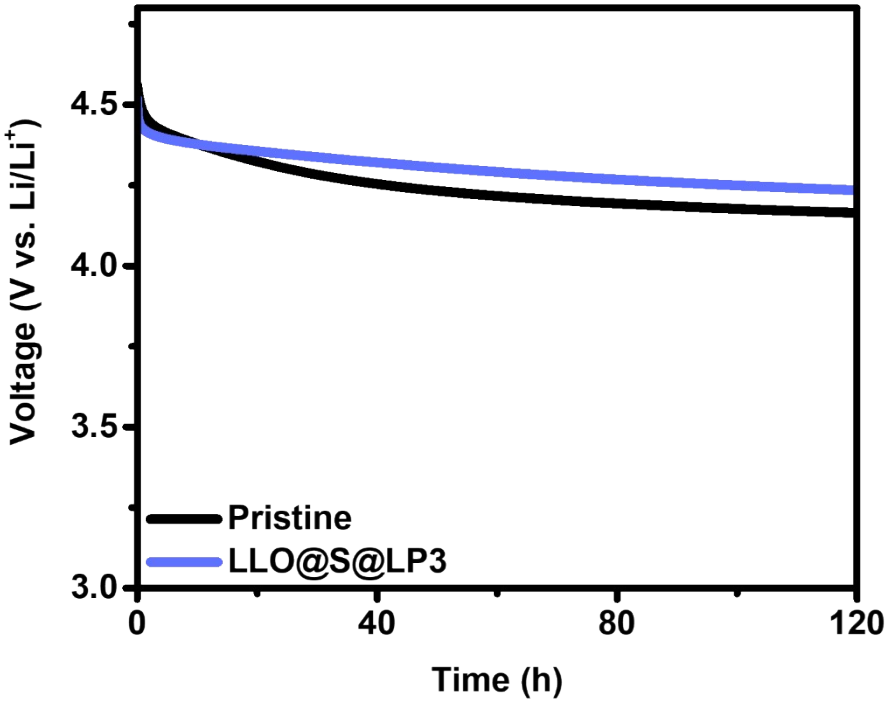

Fig. S9. The high temperature storage at 60 ℃ for 5 days.

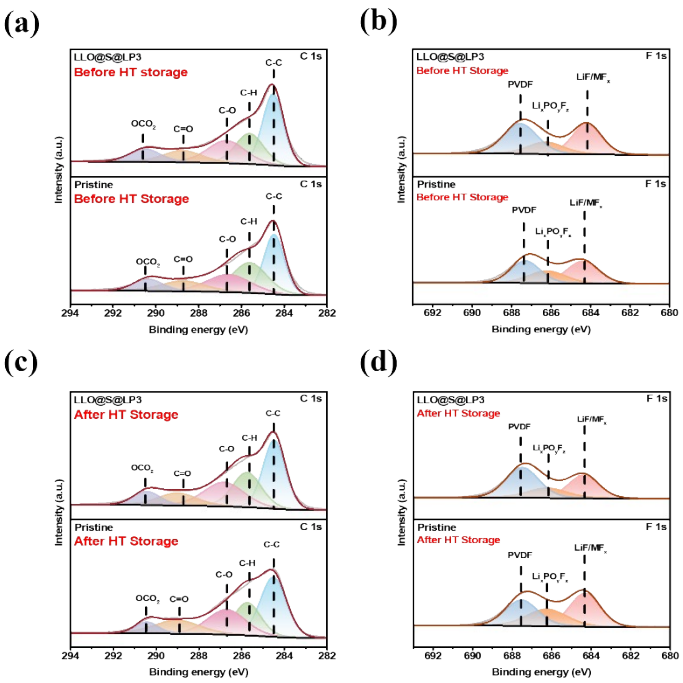

Fig. S10. X-ray photoelectron spectroscopy (XPS) spectra of the (a) C 1s, and (b) F 1s, for the pristine and LLO@S@LP3 before HT Storage, and XPS spectra of the (c) C1s, and (d) F 1s, after HT Storage.

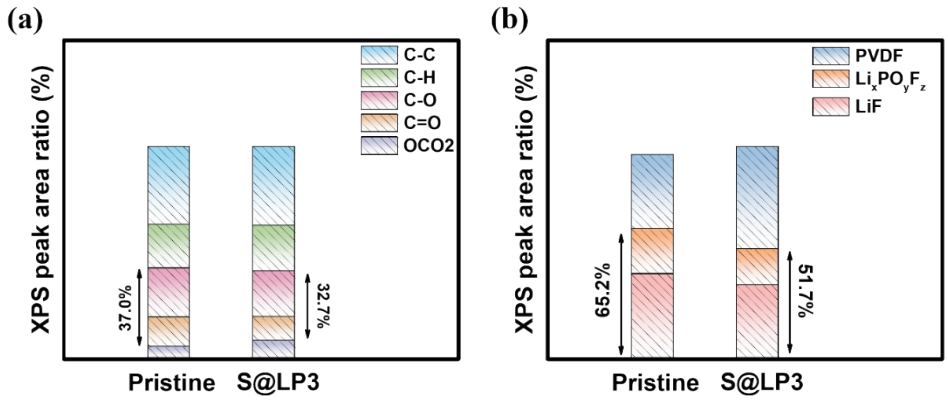

Fig. S11. After HT storage XPS peak area ratio between the Pristine and LLO@S@LP3: the

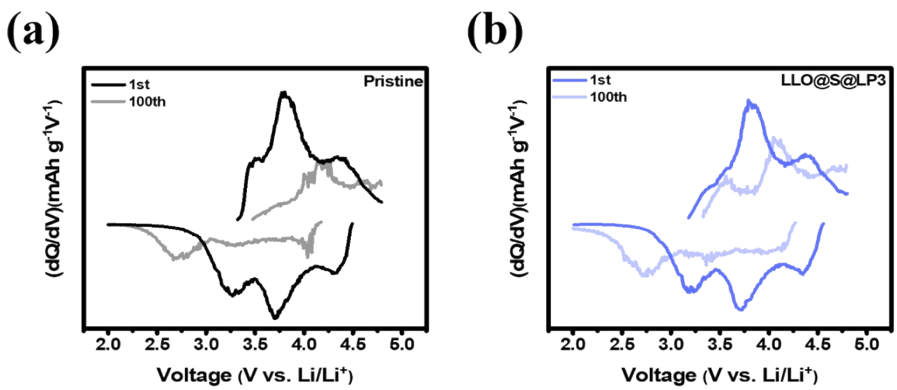

(a) C 1s, and (b) F 1s.

Fig. S12. dQ/dV plots of 1st and 100th high-temperature cycles (a) Pristine and (b) LLO@S@LP3

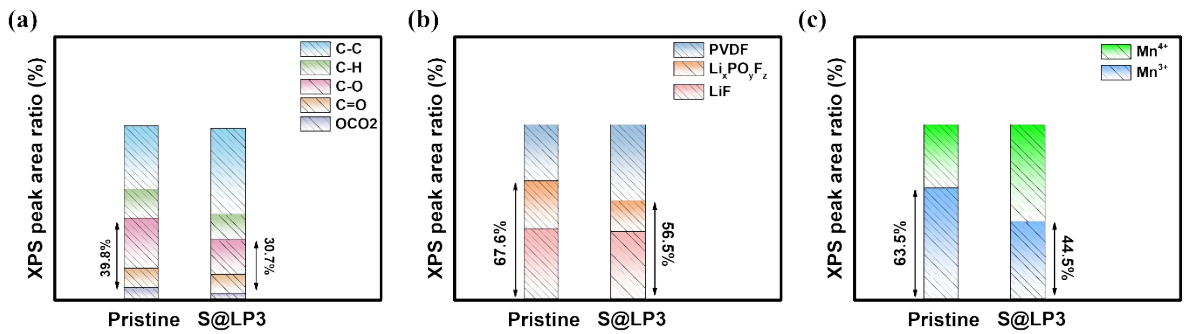

Fig. S13. After HT cycling XPS peak area ratio between the Pristine and LLO@S@LP3: the (a) C 1s, (b) F 1s, and (c) Mn 2p.

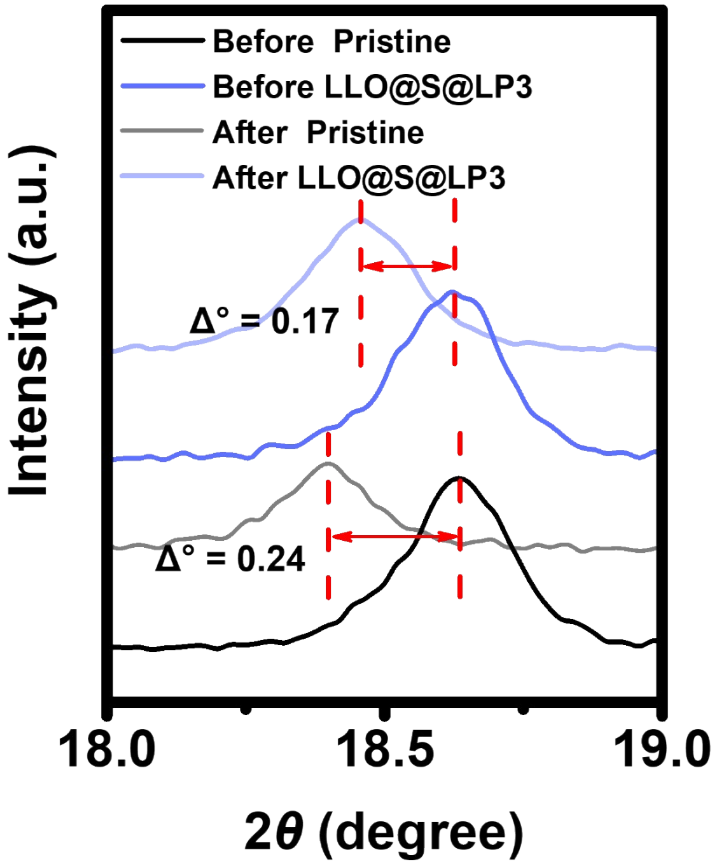

Fig. S14. After HT cycling (003) peak shifting.

Table S1. Lattice parameters of the Pristine, LLO@S@LP1, LLO@S@LP3, and LLO@S@LP5 from XRD Rietveld refinement.

Samples			Pristine	S@LP1	S@LP3	S@LP5
Lattice parameters[Å]	R-3m	a_{hex}	2.86651	2.86889	2.86860	2.86895
		c_{hex}	14.2644	14.2663	14.2717	14.2733
		c/a	4.97622	4.97389	4.97514	4.97388
	C2/m	a_{mon}	4.92993	4.90244	4.89149	4.87902
		b_{mon}	8.48489	8.48403	8.63396	8.62571
		c_{mon}	5.01765	4.92720	5.08212	5.08867
	Fd-3m	a_{cub}		8.24323	8.24363	8.23523
Reliability factors	Rwp		3.78	3.47	3.66	4.36
	Rp		3.02	3.09	2.89	3.39
	χ^2		1.20	1.26	1.38	1.58

Table S2. First cycle Charge/Discharge Capacities and Coulombic efficiencies at 0.1 C, (2.0 − 4.8) V (*vs.* Li/Li^+).

Samples	Charge capacity ($mAh\ g^{-1}$)	Discharge capacity ($mAh\ g^{-1}$)	Coulombic Efficiency (%)
Pristine	304.1	250.9	82.5
LLO@S@LP1	297.9	252.2	84.7
LLO@S@LP3	281.6	253.2	90.0
LLO@S@LP5	272.6	248.5	91.1

Table S3. Full-cell First cycle Charge/Discharge Capacities and Coulombic efficiencies at 0.1 C, (2.0 − 4.8) V (*vs.* Li/Li^+).

Samples	Charge capacity ($mAh\ g^{-1}$)	Discharge capacity ($mAh\ g^{-1}$)	Coulombic Efficiency (%)
LLO	315.5	253.0	80.2
LLO@S@LP3	286.0	253.8	88.7

Table S4. Fitting results of the EIS spectra before and after HT cycle test for the Pristine and LLO@S@LP3.

Samples	After formation			After HT cycles		
	R_s (Ω)	R_{SEI} (Ω)	R_{ct} (Ω)	R_s (Ω)	R_{SEI} (Ω)	R_{ct} (Ω)
Pristine	1.49	15.3	260.0	1.98	214.5	1419.0
LLO@S@LP3	1.47	13.6	115.9	2.44	211.7	270.6